Journal of
Advanced Manufacturing Science and Technology
jamst@jamstjournal.com;jamst2020@126.com
www.jamstjournal.com

Design and contact force analysis of the on-orbit assembly interface for stealth satellites

Andi SHE, Kan ZHENG*, Wenjie LV

School of Mechanical Engineering, Nanjing University of Science and Technology, Nanjing 210094, China

Received 25 October 2024; revised 21 November 2024; accepted 30 December 2024; Available online 25 February 2025

Abstract: Due to the unique configuration of the stealth satellite, the spatial utilization of the carrying space is very low. The need of research on on-orbit assembly technology for stealth satellites is urgent. Based on the parameters and design requirements of in-orbit assembly for stealth satellites, the on-orbit assembly interface between stealth satellite modules is designed. In a microgravity environment where loads are not easily dissipated, excessive contact forces for on-orbit assembly affect the attitude stability of the spacecraft with the on-orbit assembly platform. Based on the geometric shapes of the components in contact during the assembly process, classify contact phases and calculate the Hertz contact force. Three feed paths are set, then the trend of the contact force magnitude and the location where the maximum contact force occurs for three paths are analyzed. The contact force experiment is carried out and results are compared with analyzed results. The correctness of the trend of the magnitude of the contact forces, the maximum contact forces and the location where the maximum contact forces occurs are verified.

Keywords: stealth satellite; on-orbit assembly; assembly interface; contact force; Hertz contact force

1. Introduction

Stealth satellites have higher survivability in space conflicts compared to conventional satellites. In order to achieve high performance stealth, the stealth satellite often has a unique shape. This leads to significant constraints on the utilization of the carrier envelope space. At the same time, as the performance of stealth satellites improves, the original delivery conditions can't meet the requirements of whole-star delivery. On-orbit assembly of stealth satellites can effectively solve the above problems. In addition, compared with re-launching satellites, in-orbit servicing technology saves a great deal of human and material resources, reduces satellite maintenance costs and improves service efficiency[1].

Crossed skirt antiradar screen structure for space vehicles utilize their spreading characteristics to surround space vehicles with spreading solar arrays[2]. The dihedral shape is not conducive to radar stealth. The earliest known stealth satellite Misty achieving radar stealth by the cone that oriented toward the Earth and sufficient to obscure the satellite[3]. The system of Misty is only suitable for large satellites and only utilizes the shape to achieve radar stealth. TX 1 also utilizes a cone shape for radar stealth[4,5].

Cone-rod docking mechanisms and their derivatives are widely used in the field of on-orbit assembly. Until now, Russian spacecraft still dock with the ISS this way[6]. Interfaces for on-orbit replacement units on the International Space Station are cone-rod docking and claw-capture schemes[7]. Liu et al. designed a conical guided symmetric interface for on-orbit assembly[8]. The interface is similar to the HOTDOCK standard interface of MOSAR[9]. German team designed a spacecraft building block. Its docking interface utilized a screw and nut for expansion and contraction[10,11]. Huang et al. designed a cone-rod docking mechanism using the conical shape of a satellite engine nozzle[12]. NovaWurks was funded by the Defense Advanced Research Projects Agency to develop an articulated and astronaut-assembled satellite[13]. European Space Agency designed standard fuel filling interface for European robotic on-orbit support service[14]. The docking mechanism was similar to a cone-rod docking mechanism and the mechanism reducing assembly impact was designed at the top of the rod. Shi Chuang et al designed the on-orbit assembly unit and docking interface of a space large structure[15]. Zhao et al. designed the end effector of the on-orbit building robot with four guide flaps[16,17]. The docking interface is similar to the heterogeneous homogeneous peripheral docking mechanism used for space station segment docking. In remote sensing satellite platform for on-orbit assembly Zhao et al. proposed, a similar low-impact assembly interface is used between transfer load platforms and parent structure stars[18]. Underwood et al. designed an assembly interface driven by solenoids for the demonstration of the autonomous assembly of a reconfigurable space telescope[19].

This paper designs the on-orbit assembly interface program according to the structure and assembly conditions of the on-orbit assembly stealth satellite. The assembly contact force is the force that

* Corresponding author. *E-mail address:* zhengkan@njust. edu. cn (Kan ZHENG)
Peer review under responsibility of Editorial Committee of JAMST
DOI: 10.51393/j.jamst.2025023

have to be overcome during the assembly process. Contact forces need to be kept within reasonable limits when robots are involved in the manufacturing process[20]. Calculate Hertz contact forces based on the design of the on-orbit assembly interface. Set up 3 feed paths and then simulate and analyze the change of dimensions of contact forces. Conduct contact force experiments by a robotic arm executing the feeding of components. The change in dimensions of contact forces is measured by means of a sensor at the end of the robotic arm.

2. Design of on-orbit assembly interface for stealth satellite

2.1. Design conditions

As mentioned earlier, the cloaking shield of stealth satellites generally has a cone shape. Adjust the shape of the cloak based on the simulation results of radar cross section and on-orbit assembly requirements. Eventually, the stealthy satellite shown in Fig. 1 is obtained. The stealth satellite consists of 4 stealth plates and the satellite body. The cloaking shield consisting of 4 stealth plates. Stealth shield realizes radar stealth and visible light stealth in the direction of the Earth. Any parts can't be mounted on the Earth-facing side of the stealth plate, because they could jeopardize stealth properties. The satellite body is the 3U standard cube satellite, so it can provide 4 rails as mounting positions for its connection.

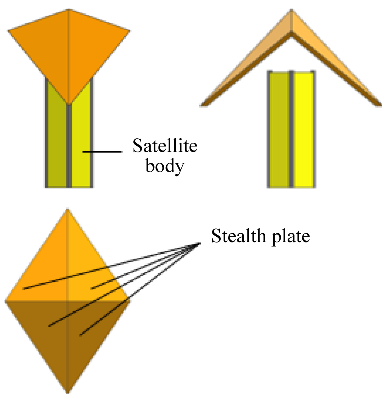

Fig. 1. Components of a stealth satellite.

The planned assembly scenario is that a space robotic arm of the on-orbit assembly platform assembles stealth plates to the satellite body that is secured to the platform. Positional and angular accuracy of 5 mm and 3° at the end of the space robotic arm, respectively. Maximum contact forces during assembly are required to be less than 80 N and more than 10 N. The lower limit of the contact force guarantees the locking force on the assembled part. Spacecraft attitude is the basis for determining the functions and work of spacecraft for all types of applications. When a spacecraft is subjected to force, its attitude changes. Wrong attitude will lead to spacecraft safety accidents. The spacecraft controls its attitude by means of momentum wheels, magnetic torque machines, gas propulsion and electric propulsion. It takes a while for these devices to adjust the spacecraft's uncontrolled attitude correctly. This explains why loads are not easily dissipated in microgravity environments. Both the on-orbit assembly platform and the space robot arm work on the spacecraft. Excessive on-orbit assembly contact forces affect the attitude stability of the spacecraft. Therefore, set the upper limit of the contact force. Dimensions of each component are known.

2.2. Design of on-orbit assembly interface

Assembly interfaces can be categorized into the passive part which generally a simple design is preferable for and the master part which a complicated design is preferable for[21]. As mentioned earlier, the on-orbit assembly interface is generally a cone-rod docking mechanism or a similar cone-rod docking mechanism. However, the cone-rod docking mechanism is not suitable for the on-orbit assembly between the stealth plate and the satellite body. The similar cone-rod docking mechanism requires a large mounting and working space. In the previously described on-orbit assembly scenario using the cone-rod docking mechanism, alongside the assembly interface there will be an active locking mechanism matching it. The active locking mechanism in turn requires a motor as a power source. The complete docking mechanism requires considerable installation and working space. Therefore, this type of docking mechanism is not suitable.

The space robotic arm that serves as the power source for the assembly can only perform simple movement operations. The designed assembly interface should meet the requirement that the space robotic arm can complete the assembly by simply moving. Consider that space robotic arm is not necessarily equipped with the flexible control system and flexible joints. The design of the assembly interface requires assembly error compensation. This further reduces requirements for the space robotic arm.

The on-orbit assembly design of the stealth plate is shown in Fig. 2. The non-Earth-facing side of the stealth plate is fitted with an insert plate for assembly and a handle gripped by the space robotic arm. Four stealth plates are with the same design.

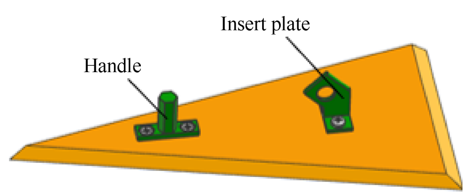

Fig. 2. On-orbit assembly design of the stealth plate.

The on-orbit assembly design of the satellite body is shown in Fig. 3. Two assembly interface components are attached to the satellite body by means of a bracket. The design of the assembly interface component is shown in Fig. 4, including the base plate, the cover plate, the torsion spring and the cone head rod. The entire assembly interface is a mechanical interface with a movable part for high reliability.

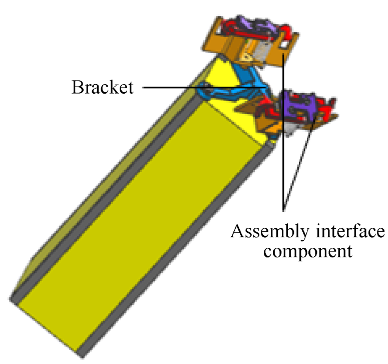

Fig. 3. On-orbit assembly design of the satellite body.

The assembly process is shown in Fig. 5. Hide stealth plates for better presentation of the process. The assembly process of the assembly interface consists of moving the stealth plate with the insert plate towards the assembly interface component under the control of the space robotic arm. The insert plate makes contact with the cone head rod and pushes the cone head rod to rotate. As the insert plate is fed, the apex of the cone head rod will slide into the hole of the insert plate. Finally, the insert plate will make contact with the base plate. The force sensor of the space robotic arm senses that the contact force has reached the set value, then the space robotic arm loosens the stealth plate. Under the action of the torsion spring, the taper bar returns to its original position and drives the insertion plate to the specified position. Thus, eliminating assembly deviations are eliminated.

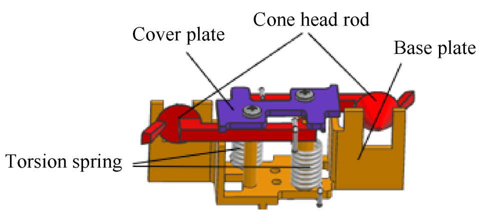

Fig. 4. Design of the assembly interface component.

The on-orbit assembly is divided into two stages: positioning and locking. This solution combines positioning and locking in one process. The process of locking is also the process of positioning. In order to compensate for assembly deviations, the position of one of the assembled parties needs to be continuously adjusted. Therefore, the space robotic arm will loosen the stealth plate at the end of phase 4 shown in Fig. 5, and the compensation of assembly deviations will be completed automatically by the assembly interface.

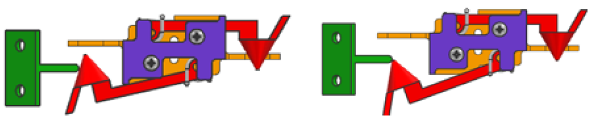

(a) Phase 1 (b) Phase 2

(c) Phase 3 (d) Phase 4

Fig. 5. Assembly process.

3. Assembly contact force calculation

Because the working environment is a microgravity environment, the forces that need to be overcome for on-orbit assembly are mainly contact forces during assembly. Dimensions of contact forces needs to meet the design requirements. The contact force is also an input condition for the dynamics analysis of the on-orbit assembly platform and its space robotic arm. Thus, solving for contact forces is necessary.

The Taylor expansion of the binary function Taylor expansions of binary functions that will be encountered during the solution process is

$$f(x,y)=f(x_0,y_0)+(x-x_0)f_x'(x_0,y_0)+(y-y_0)f_y'(x_0,y_0)+\frac{1}{2!}(x-x_0)^2f_{xx}''(x_0,y_0)+\frac{1}{2!}(x-x_0)(y-y_0)f_{xy}''(x_0,y_0)+\frac{1}{2!}(x-x_0)(y-y_0)f_{yx}''(x_0,y_0)+\frac{1}{2!}(y-y_0)^2f_{yy}''(x_0,y_0)+\cdots+o^n \tag{1}$$

As shown in Fig. 5, based on the geometry of the contact between the insert plate and the cone head rod, the contact can be divided into 4 phases. Phase 1 is when the cylindrical surface of the insert plate comes into contact with the conical surface of the cone head rod. Phase 2 is the cylindrical surface of the insert plate comes into contact with the spherical surface of the apex of the cone head rod. Phase 3 is the contact between the spherical surface of the apex of the cone head rod and the flat surface of the insert plate. Phase 4 is the contact between the circular surface formed by the inverted circle of the insert plate and the conical surface of the cone head rod.

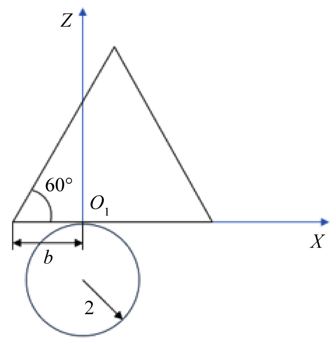

Fig. 6. Schematic of phase 1 contact.

Solve the Hertz contact force equation for phase1. As shown in Fig. 6, establish a coordinate system O_1 based on the cylindrical cross-section and the conical cross-section with the contact point as the origin. The radius of the cross-section of the cylinder is 2 mm. The angle of the top of the cone is 60°. The equation of the conic surface in the coordinate system O_1 is

$$z^2-\sqrt{3}\,(x+b)z+\frac{3}{2}y^2=0 \tag{2}$$

According to the root formula of the quadratic equation, the distance z_{co} from the point near the contact point on the conic surface to the XY plane is

$$z_{co}(x,y)=\frac{\sqrt{3}\,(x+b)-\sqrt{3(x+b)^2-6y^2}}{2} \tag{3}$$

where b is the distance from the apex of the cone to the contact point, varying with time.

The distance z_{cy} from the point near the contact point on the cylindrical plane to the XY plane is

$$z_{cy}(x,y)=2-\sqrt{4-x^2} \tag{4}$$

A binary function Taylor expansion of the two functions $z_{co}(x, y)$ and $z_{cy}(x, y)$ at the point (0,0), ignoring terms more than three times, yields

$$z_{co}=\frac{\sqrt{3}}{2b}y^2 \tag{5}$$

$$z_{cy}=\frac{1}{4}x^2 \tag{6}$$

The distance between the point on the cylindrical surface and the point on the conical surface in the direction normal to the contact surface is

$$z_{co}+z_{cy}=\frac{\sqrt{3}}{2b}y^2+\frac{1}{4}x^2 \tag{7}$$

From Eq. (7), the radius of principal curvature of the equivalent space geometry at the contact point is $b/\sqrt{3}$ and 2.

The equivalent Gaussian curvature radius is

$$R_1=\sqrt{\frac{b}{\sqrt{3}}\cdot 2}=\sqrt{\frac{2\sqrt{3}\,b}{3}} \tag{8}$$

The equivalent modulus of elasticity E^* is expressed as[22]

$$\frac{1}{E^*}=\frac{1-v_1^2}{E_1}+\frac{1-v_2^2}{E_2} \tag{9}$$

E_1 and E_2 are the modulus of elasticity of the two objects, respectively. v_1 and v_2 are the Poisson's ratios of the two objects, respectively.

The insert plate and the cone head rod are made of 6061 with a Poisson's ratio of 0.3[23]. The modulus of elasticity[24] is 69×10^3 N/mm^2.

The Hertz contact force equation is[22]

$$F=\frac{4}{3}E^*R^{\frac{1}{2}}d^{\frac{3}{2}} \tag{10}$$

where d is the indentation depth. Substituting Eq. (8) into Eq. (10), the equation for the Hertz contact force F_1 at phase 1 is given by

$$F_1=\frac{2^{\frac{9}{4}}}{3^{\frac{9}{8}}}E^*b^{\frac{1}{4}}d^{\frac{3}{2}} \tag{11}$$

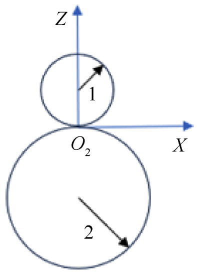

Fig. 7. Schematic of phase 2 contact.

Solve the Hertz contact force equation for phase 2. As shown in Fig. 7, the coordinate system O_2 is established based on the cylindrical cross-section and the spherical cross-section with the contact point as the origin. The radius of the spherical surface at the apex of the cone is 1 mm.

The distance z_{sp} from a point near the contact point on the sphere to the XY plane is

$$z_{sp}=1-\sqrt{1-x^2-y^2} \tag{12}$$

A binary Taylor expansion of the function $z_{sp}(x,y)$ at the point (0, 0), ignoring terms more than three times, yields

$$z_{sp}=\frac{x^2}{2}+\frac{y^2}{2} \tag{13}$$

The distance between the point on the cylindrical surface and the point on the spherical surface in the direction normal to the contact surface is

$$z_{cy}+z_{sp}=\frac{1}{4}x^2+\frac{x^2}{2}+\frac{y^2}{2}=\frac{x^2}{\frac{4}{3}}+\frac{y^2}{2} \tag{14}$$

From Eq. (7), the radius of principal curvature of the equivalent space geometry at the contact point is 2/3 and 1. The equivalent Gaussian curvature radius is

$$R_2=\sqrt{\frac{2}{3}\times1}=\frac{\sqrt{6}}{3} \tag{15}$$

Substituting Eq. (15) into Eq. (10), the equation for the Hertz contact force F_2 at phase 2 is given by

$$F_2=\frac{4\times6^{\frac{1}{4}}}{3\sqrt{3}}E^*d^{\frac{3}{2}} \tag{16}$$

Solve the Hertz contact force equation for phase 3. The contact between a plane and a sphere is a typical contact. According to Eq. (13), the Hertz contact force F_3 at phase 3 is

$$F_3=\frac{4}{3}E^*d^{\frac{3}{2}} \tag{17}$$

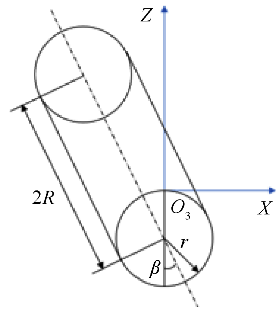

Fig. 8. Schematic of phase 4 contact.

Solve the Hertz contact force equation for phase 4. As shown in Fig. 8, the coordinate system O_3 is established based on the cross-section of the ring with the contact point as the origin. The Z-axis is the direction normal to the contact surface. The XZ plane passes through the center of the circular hole. R is the distance from the center of the circular hole to the center of the circular tube. r is the radius of the circular pipe. β is the angle between the plane of the pipe path with radius R and the Z-axis and varies with time during the contact.

In the coordinate system O_3, the equation of the circular plane is

$$r^2=(x\cos\beta+z\sin\beta+r\sin\beta)^2+\left(R-\sqrt{(x\sin\beta+R-r\cos\beta-z\cos\beta)+y^2}\right)^2 \tag{18}$$

The distance from the point near the contact point on the circular surface to the XY plane can't be obtained directly by Eq. (18). It is straightforward to find the partial derivative of Eq. (18) at the point (0,0), which is given by

$$z_x(0,0)=0 \tag{19}$$

$$z_y(0,0)=0 \tag{20}$$

$$z_{xx}(0,0)=\frac{1}{r} \tag{21}$$

$$z_{yy}(0,0)=\frac{\cos\beta}{R-r\cos\beta} \tag{22}$$

Thereby, the Taylor expansion of the binary function of the distance z_{to} the contact plane from the point near the contact point on the circular surface is obtained.

$$z_{to}=\frac{x^2}{2r}+\frac{y^2}{\frac{2(R-r\cos\beta)}{\cos\beta}} \tag{23}$$

Eq.(5) is known to be the equation for the distance from a point near the point of contact on a conic surface to the plane of contact. The coordinate system based on Eq.(23) is obtained by angling γ around the Z-axis to obtain the coordinate system based on Eq.(5). Eq.(23) is based on a coordinate system in which the equation for the distance from a point near the contact point on the conic plane to the contact plane is

$$z_{co}=\frac{\sqrt{3}\cos^2\gamma}{2b}y^2-\frac{\sqrt{3}\sin\gamma\cos\gamma}{b}xy+\frac{\sqrt{3}\sin^2\gamma}{2b}x^2 \tag{24}$$

Combining Eq. (23) and Eq. (24), the distance formula z_{tc} from the circular surface to the conical surface is

$$\begin{aligned} z_{tc}&=z_{to}+z_{co}\\ &=\frac{b+\sqrt{3}\sin^2\gamma}{2rb}x^2-\frac{\sqrt{3}\sin\gamma\cos\gamma}{b}xy+\\ &\quad\frac{b\cos\beta+\sqrt{3}(R-r\cos\beta)\cos^2\gamma}{2b(R-r\cos\beta)}y^2 \end{aligned} \tag{25}$$

In order to turn the above quadratic into a standard quadratic (to obtain the principal curvatures), find its eigenvalues λ.

$$\frac{\sqrt{3}\,br\cos 2\gamma\cos\beta}{4b^2 r(R-r\cos\beta)} = \frac{b^2\cos\beta+\sqrt{3}\,Rb\cos^2\gamma}{4b^2 r(R-r\cos\beta)} + \lambda^2 - \frac{bR+\sqrt{3}\,Rr-\sqrt{3}\,r^2}{2rb(R-r\cos\beta)}\lambda \tag{26}$$

Suppose

$$k_1 = \frac{bR+\sqrt{3}\,rR-\sqrt{3}\,r^2}{2rb(R-r\cos\beta)} \tag{27}$$

$$k_2 = \frac{b^2\cos\beta+\sqrt{3}\,Rb\cos^2\gamma}{4b^2 r(R-r\cos\beta)} - \frac{\sqrt{3}\,br\cos 2\gamma\cos\beta}{4b^2 r(R-r\cos\beta)} \tag{28}$$

The eigenvalues λ_1 and λ_2 can be obtained from the rooting formula.

$$\lambda_1 = \frac{-k_1-\sqrt{k_1^2-4k_2}}{2} \tag{29}$$

$$\lambda_2 = \frac{-k_1+\sqrt{k_1^2-4k_2}}{2} \tag{30}$$

The two eigenvalues above are the principal radii of curvature of the equivalent space geometry at the point of contact. Therefore, the equivalent Gaussian curvature radius is

$$R_2 = \sqrt{\frac{2}{-k_1-\sqrt{k_1^2-4k_2}}\cdot\frac{2}{-k_1+\sqrt{k_1^2-4k_2}}} = \frac{1}{\sqrt{k_2}} \tag{31}$$

Substituting Eq. (31) into Eq. (10), the equation for the Hertz contact force F_4 at phase 4 is

$$F_4 = \frac{4}{3}E^* k_2^{-\frac{1}{4}} d^{\frac{3}{2}} \tag{32}$$

4. Contact force simulation analysis

The three feed paths tested in the simulation are shown in Fig. 9. Other parts are hidden for better presentation. Path 1 is the standard path. Both path 2 and path 3 have a positional deviation of 5 mm and an angular deviation of 3° with respect to path 1.

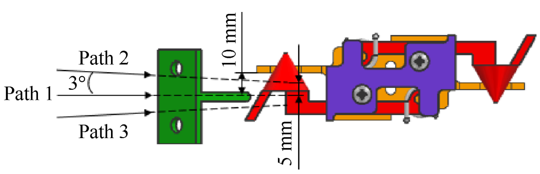

Fig. 9. Feed path.

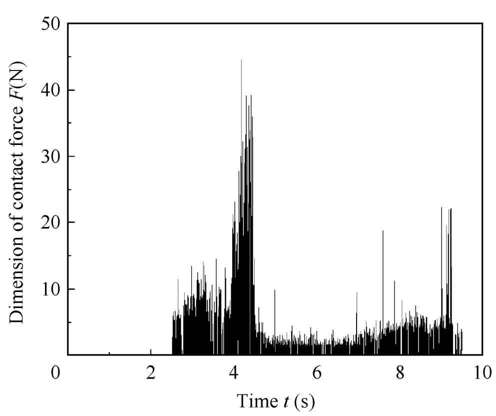

Fig. 10. Dimensions of simulated contact forces under path 1.

Dimensions of the contact force on the insertion plate obtained from the simulation under the conditions of path 1, path 2 and path 3 are shown in Figs. 10, 11 and 12, respectively. As can be seen from these line plots, the contact force simulation results vary dramatically between 0 and non-0. This condition is caused by vibration of the cone head rod. In addition, the vibration of the cone head rod caused a number of discrete points to appear in the contact force simulation results.

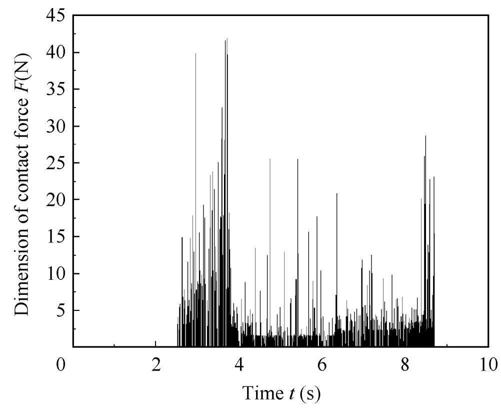

Fig. 11. Dimensions of simulated contact forces under path 2.

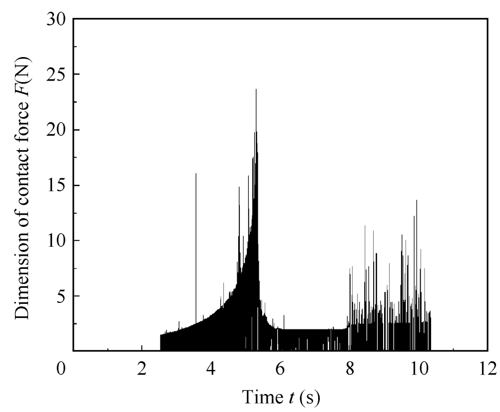

Fig. 12. Dimensions of simulated contact forces under path 3.

Although the discrete points have some influence on the results of the contact force simulation, the time when the contact force is the largest in the overall view is the moment when the contact ends in phase 1. The phases that level off in the middle are phases 2 and 3, which are the same as the calculations. The dimension of the maximum contact force satisfies the design requirements whether or not discrete results are considered.

5. Experimental analysis of contact forces

Dimensions of contact forces exerted on the experimentally measured insertion plate for path 1, path 2 and path 3 conditions are shown in Figs 14, 15 and 16, respectively. From the results pre-

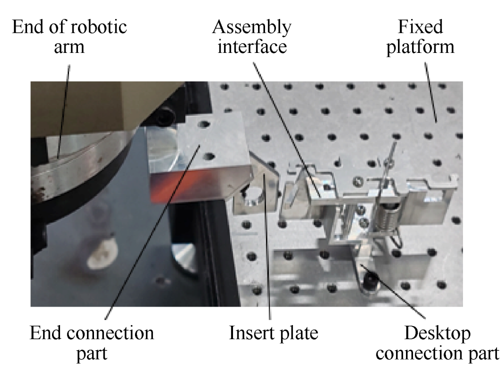

Fig. 13. Contact force measurement experiment

sented in the figures, it can be seen that the execution of the feed by the robotic arm already affects the sensors before contact occurs.

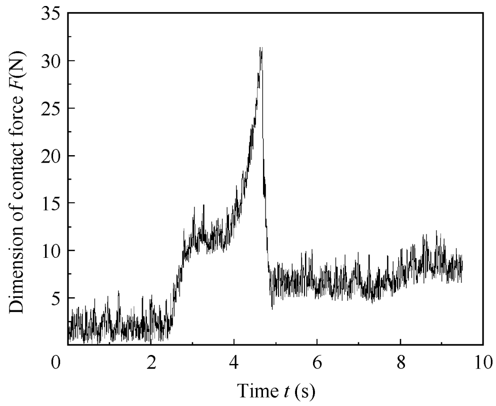

Fig. 14. Dimensions of experimental contact forces under path 1.

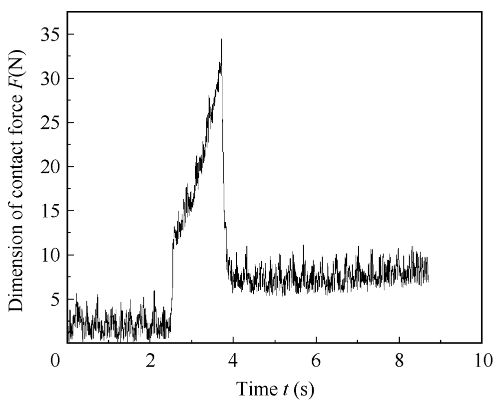

Fig. 15. Dimensions of experimental contact forces under path 2.

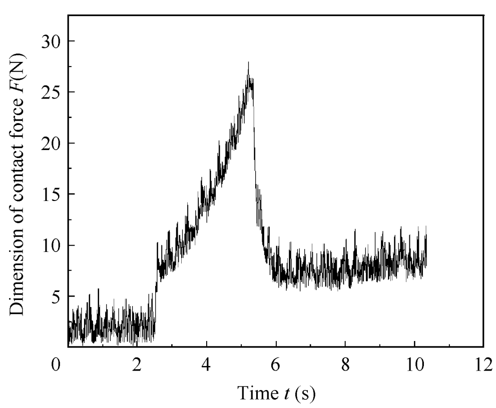

Fig. 16. Dimensions of experimental contact forces under path 3.

6. Comparison of results

Because of the deviation between the manually measured experimental path and the simulated path, the contact start time for the experiment is slightly different from the contact start time for the simulation.

The similarities between two results are the trend of the contact force and the location where the maximum contact force occurs. For the trend of the change in the dimension of the contact force, experimental results are the same as simulation results. The maximum contact forces all occur at the moment of the end of the contact in phase 1. The curve of the dimension of the contact force tends to flatten out in phase 2 and phase 3. A small increase in the dimension of the contact force occurs in phase 4. Dimensions of maximum contact forces for the 3 paths meet the design requirement.

The differences are that the contact force obtained from the experiment is larger than that obtained from the simulation and simulation results oscillate more violently than experimental results. Next, the reasons for such differences are analyzed. The contact force obtained from the experiment is larger than the one obtained from the simulation should be the result of the path error, the error of the sensor and the friction that is not sufficiently taken into account in the simulation. The damping in the simulation environment does not exactly match the damping in the actual environment, making simulation results oscillate more violently than experimental results.

7. Conclusion

This paper takes the on-orbit modularized assembly of stealth satellite as the starting point to complete the design of the on-orbit assembly interface and contact forces analysis of the stealth satellite. According to results of simulation analysis and experimental analysis, the following conclusions can be obtained:

(1) The simulation presents same trends of change in contact forces as presented by the experiment. The drastic change in contact forces occurs during assembly phase 1. The change in contact forces tends to level off during assembly phase 2 and assembly phase 3. A small increase in the dimension of the contact force occurs in phase 4.

(2) The maximum contact force occurs at the moment of the end of the contact in phase 1. Both simulated and experimental maximum contact forces satisfy the requirements in the range of 10 N to 80 N.

(3) The path error, the error of the sensor and the friction that is not sufficiently taken into account in the simulation make the contact force obtained from the experiment larger than that obtained from the simulation. The contact force simulation results vary dramatically between 0 and non-0. The damping in the simulation environment does not exactly match the damping in the actual environment, making simulation results oscillate more violently than experimental results. The contact force simulation of the assembly interface is only suitable for verifying contact force trends.

References

1. Fan XY, Bi JF, Chu M. An improved Yolov7-tiny model for modular satellite component identification. *Journal of Advanced Manufacturing Science and Technology* 2025;5(3):2025014.
2. Willam CB, Donald MS. Crossed skirt antiradar screen structure for space vehicles[P]. US: 6107952, 1971-1-4.
3. Morton TE, Karl HM, Richard M H. Satellite signature suppression shield [P]. US: 5345238, 1990-5-14.
4. Zhou Y, Xu YG, Ye HX. A Integrated design for structure and EM stealth of microsatellite. *2021 International Conference on Microwave and Millimeter Wave Technology*; 2021 May 23-26; Nanjing, China. New York: IEEE;2021. p. 1765-1767.
5. Hu HB, Zhang X, Liao WH, et al. Progress and prospect in satellite stealth technology. *Journal of National University of Defense Technology* 2021; 43(3):107-127 [Chinese].
6. Ma S, Feng X, Kong N, et al. Review and development prospect of space rendezvous and docking mechanism. *Journal of Rocket Propulsion* 2022;48(3):1-15 [Chinese].
7. Rembala R, Ower C. Robotic assembly and maintenance of future space stations based on the ISS mission operations experience. *Acta*

Astronautica 2009;65(7-8): 912-920.

8. Liu S, Zhang EY, Xu ZB, et al. Design of docking interfaces for on-orbit assembly of large structures in space. *Sensors* 2024; 24(20):6534.
9. Nair MH, Rai MC, Poozhiyil M, et al. Robotic technologies for in-orbit assembly of a large aperture space telescope: A review. *Advances in Space Research* 2024;74(10):5118-5141.
10. Schervan TA, Kreisel J, Schroeder KU, et al. New horizons for exploration via flexible concepts based on building blocks using the standardized ISSI (intelligent space system interface) modular coupling kit by iBOSS. *Global Space Exploration Conference 2021*;2021 June 14-18; St. Petersburg, Russia. Paris: IAF;2021. p. 14-18.
11. Kortman M, Ruhl S, Weise J, et al. Building block based iBOSS approach: fully modular systems with standard interface to enhance future satellites. *66th International Astronautical Congress*; 2015 October 12-16; Jerusalem Israel. Paris: IAF;2015; 2(15):1-11.
12. Huang FB, Li Z, Huang LF, et al. Docking mechanism design and dynamic analysis for the GEO tumbling satellite. *Assembly Automation* 2019;39(3):432-444.
13. Helms C C. A survey of launch services 2016-2020. *AIAA Propulsion and Energy 2020 Forum*; 2020 August 24-28. Reston: AIAA; 2020. p. 3532.
14. Medina A, Tomassini A, Suatoni M, et al. Towards a standardized grasping and refuelling on-orbit servicing for geo spacecraft. *Acta Astronautica* 2017;134: 1-10.
15. Shi C, Li WJ, Guo HW, et al. Research on on-orbit assembly unit and docking interface of large space structure. *Journal of Mechanical Engineering* 2022;58(01): 52-60[Chinese].
16. Zhao LL, Liu ZY, Zhao JD, et al. Design and verification of end-effector and adaptation interfaces for on-orbit construction of space robot. *Journal of Mechanical Engineering* 2024;60(3): 1-10[Chinese].
17. Zhao JD, Wang ZR, et al. Model Design and Concept of Operations of Standard Interface for On-orbit Construction. *2024 IEEE International Conference on Robotics and Automation*, 2024 May 13-17; Yokohama, Japan. New York: IEEE, 2024. p. 13487-13493.
18. Zhao XG, Li WL, Zhao C, et al. Overall design of remote sensing large-platform satellite for on orbit assembly and maintenance. *Ninth Symposium on Novel Photoelectronic Detection Technology and Applications*; 2023 April 21-23; Hefei, China. Bellingham: SPIE; 2023. p. 594-600.
19. Underwood C, Pellegrino S, Lappas V J, et al. Using CubeSat/micro-satellite technology to demonstrate the Autonomous Assembly of a Reconfigurable Space Telescope. *Acta Astronautica* 2015;114: 112-122.
20. Yu Y, Wang RQ, Wang YP, at el. Contact force controlled robotic polishing for complex PMMA parts with an active end-effector. *Journal of Advanced Manufacturing Science and Technology* 2021; 1(4): 2021012.
21. Li WJ, Cheng DY, Liu XG, et al. On-orbit service (OOS) of spacecraft: A review of engineering developments. *Progress in Aerospace Sciences* 2019;108: 32-120.
22. Valentin L P. *Contact mechanics and friction physical principles and application*. Beijing: Tsinghua University Press; 2019. p. 47-49[Chinese].
23. Chen DX. *Handbook of mechanical design*. Beijing: Chemical Industry Press;2016. p. 1-7[Chinese].
24. GB/T 20801.2-2020. Pressure piping code—industrial piping—part 2: material[S] [Chinese].